J. Fluid Mech. (1988), *vol.* 190, *pp.* 471–489
Printed in Great Britain

Steady viscous flow past a sphere at high Reynolds numbers

By BENGT FORNBERG
Exxon Research and Engineering Company, Annandale, NJ 08801, USA

(Received 5 June 1987)

Numerical solutions are presented for steady incompressible flow past a sphere. At high Reynolds numbers (results are presented up to $R = 5000$), the wake is found to resemble a Hill's spherical vortex.

1. Introduction

Viscous flow past a circular cylinder becomes unstable around Reynolds number $R = 40$ and past a sphere around $R = 130$. We are interested in the structure of the steady (but unstable) solutions above these Reynolds numbers. Apart from studies by the present author, the upper limit for (reasonably accurate) solutions for the cylinder in the literature appears to be $R = 120$ (Ta 1975), and for the sphere $R = 400$ (Le Clair, Hamielec & Pruppacher 1970; Woo 1971).

An earlier study by the present author (Fornberg 1985, hereinafter denoted F85) describes a calculation for the cylinder up to $R = 600$. This report describes a similar calculation for the sphere, carried out up to $R = 5000$. In both cases, it is the application of Newton's method to solve the discretized equations that enabled us to obtain converged solutions well past the 'barrier' where instabilities otherwise would start to occur. Conventional iterative techniques tend, in the artificial time introduced by the iterations, to pick up instabilities reminiscent of temporal ones. The quadratic convergence of Newton's method precludes this from happening. With the present evolution of supercomputers, the computational cost of this approach is no longer prohibitive.

In the case of a cylinder, the wake bubble (the region with recirculating flow) was found to increase linearly with R in both length and width above $R \approx 300$. In the sphere case, both growth rates are much lower, possibly like $\log R$. In both cases, it appears likely that very high-Reynolds-number wake bubbles will be large, wide and similar in structure to Euler solutions which can translate through the fluid without any bodies present.

Portions of this work have appeared in preliminary form as part of a conference contribution (Fornberg 1987).

2. Mathematical formulation

With a sphere of radius one and the Reynolds number based on the diameter, the steady-state Navier–Stokes equations in cylindrical coordinates take the form

$$\frac{\partial^2 \Psi}{\partial x^2} + \frac{\partial^2 \Psi}{\partial y^2} - \frac{1}{y}\frac{\partial \Psi}{\partial y} + y\omega = 0, \tag{1}$$

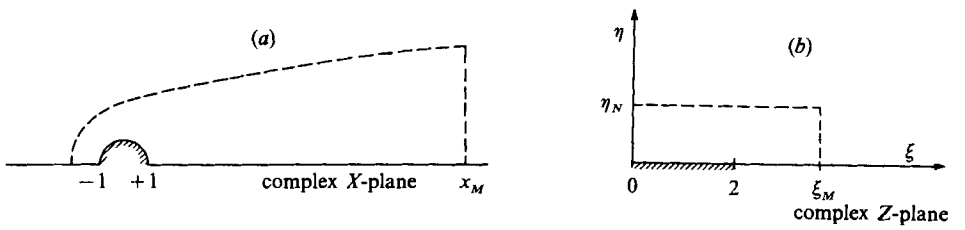

FIGURE 1. Computational domain in (*a*) the physical X-plane and (*b*) its image in the Z-plane.

$$\frac{\partial^2\omega}{\partial x^2}+\frac{\partial^2\omega}{\partial y^2}+\frac{1}{y}\frac{\partial\omega}{\partial y}-\frac{\omega}{y^2}-\frac{R}{2y}\left\{\frac{\partial\Psi}{\partial y}\frac{\partial\omega}{\partial x}-\frac{\partial\Psi}{\partial x}\frac{\partial\omega}{\partial y}+\frac{\omega}{y}\frac{\partial\Psi}{\partial x}\right\}=0. \tag{2}$$

Here, Ψ denotes a stream function and ω vorticity. The x-axis is the downwind symmetry axis and y the distance from this axis.

Near the sphere, all the vorticity is concentrated within a region similar to the one sketched in figure 1(*a*). The conformal mapping

$$Z=X^{\frac{1}{2}}+X^{-\frac{1}{2}} \tag{3}$$

maps such regions in the physical $(X=x+\mathrm{i}y)$-plane to rectangles in the $(Z=\xi+\mathrm{i}\eta)$-plane (figure 1*b*). After an arbitrary conformal mapping, the governing equations (1), (2) take the form

$$\left\{\frac{\partial^2\Psi}{\partial\xi^2}+\frac{\partial^2\Psi}{\partial\eta^2}\right\}J(\xi,\eta)+\frac{1}{y}\left\{\eta_x\frac{\partial\Psi}{\partial\xi}-\xi_x\frac{\partial\Psi}{\partial\eta}\right\}+y\omega=0, \tag{4}$$

$$\left\{\frac{\partial^2\omega}{\partial\xi^2}+\frac{\partial^2\omega}{\partial\eta^2}\right\}J(\xi,\eta)-\frac{1}{y}\left\{\eta_x\frac{\partial\omega}{\partial\xi}-\xi_x\frac{\partial\omega}{\partial\eta}\right\}-\frac{\omega}{y^2}$$
$$+\frac{R}{2y}\left\{\left(\frac{\partial\Psi}{\partial\xi}\frac{\partial\omega}{\partial\eta}-\frac{\partial\Psi}{\partial\eta}\frac{\partial\omega}{\partial\xi}\right)J(\xi,\eta)-\frac{\omega}{y}\left(\xi_x\frac{\partial\Psi}{\partial\xi}+\eta_x\frac{\partial\Psi}{\partial\eta}\right)\right\}=0, \tag{5}$$

where $J(\xi,\eta)=\xi_x^2+\eta_x^2$. These equations are further modified by separate changes of variables in the ξ- and η-directions:

For $0\leqslant\xi\leqslant 2$ (corresponding to the sphere surface if $\eta=0$), $\xi(\zeta)$ is a quintic satisfying

$$\left.\begin{aligned}\xi(0)&=0, & \xi(2)&=2,\\ \xi'(0)&=0.7, & \xi'(2)&=0.1,\\ \xi''(0)&=0, & \xi''(2)&=0.\end{aligned}\right\} \tag{6}$$

For $\xi\geqslant 2$, $\xi(\zeta)$ is a cubic satisfying the same conditions at $\zeta=2$ and an additional one at the outer edge of the computed domain:

$$\left.\begin{aligned}&\xi(2)=2, \quad \xi(6)=10.8,\\ &\xi'(2)=0.1,\\ &\xi''(2)=0.\end{aligned}\right\} \tag{7}$$

For $\eta\geqslant 0$, $\eta(\kappa)$ is a cubic satisfying

$$\left.\begin{aligned}&\eta(0)=0, \quad \eta(\tfrac{4}{3})=0.6,\\ &\eta'(0)=0.1,\\ &\eta''(0)=0.\end{aligned}\right\} \tag{8}$$

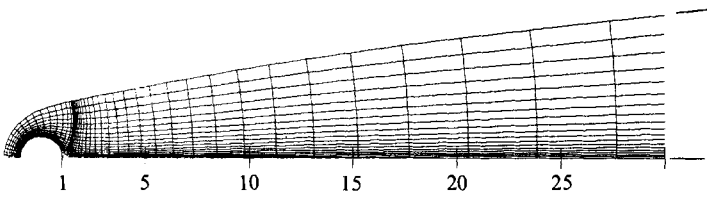

FIGURE 2. Part of the computational domain near the sphere of a rectangular grid in the Z-plane.

By varying the (non-zero) constants in these transformations, the relative grid densities in different parts of the flow field can be adjusted, for example to provide sufficient boundary-layer resolution and to 'offset' the grid singularity at the rear stagnation point on the sphere surface. In all cases presented in this work, the particular constants given above were used.

The domain size was also the same in all cases (except when changed to test for errors from boundary conditions as explained in a later section). In (ζ, κ)-space, the computational domain was $[0, 6] \times [0, \frac{4}{3}]$, corresponding in (ξ, η)-space to $[0, 10.8] \times [0, 0.6]$. Three levels of resolution were used. The equidistant mesh spacings were $(\Delta\zeta = \frac{1}{36}, \Delta\kappa = \frac{1}{54})$; $(\Delta\zeta = \frac{1}{54}, \Delta\kappa = \frac{1}{81})$; and $(\Delta\zeta = \frac{1}{81}, \Delta\kappa = \frac{2}{243})$ respectively. Denoted G1, G2 and G3, these grids were of sizes 217×73, 325×109 and 487×163 points respectively. The sequence of grids correspond to successive refinement with a factor of $\frac{2}{3}$ in each direction.

Figure 2 shows the size of the computational domain in physical space near the sphere and the effect of the transformations on the grid density. However, for best visibility, the grid displayed has only $\frac{1}{4}$ the density of G1 in each direction (i.e. it corresponds to a 55×19 grid which would be obtained by using $(\Delta\zeta = \frac{1}{9}, \Delta\kappa = \frac{2}{27})$.

3. Numerical approximation of the governing equations

The governing equations are approximated by centred second-order finite differences at all interior points. At each boundary, two conditions are supplied. At the body surface they are $\Psi = 0$ and $\partial\Psi/\partial\eta = 0$, and along the axis of symmetry $\Psi = 0$ and $\omega = 0$. At the outflow boundary, simple extrapolations proved satisfactory (as described in F85).

The vorticity decays exponentially to zero for increasing values of η. The 'top' boundary is located sufficiently far out that the vorticity on or above it can be ignored. Figure 2 shows the location used at all Reynolds numbers in this study. On this boundary, ω is set to zero. The crucial issue is which second condition to apply. At least in two dimensions, use of 'free-stream' or leading terms in far-field asymptotic expansions proves unsatisfactory even when applied at large distances. This becomes even more the case if the boundary is not uniformly far out but comes close to the sphere, as with the present grid. The following approach applies equally well to two dimensions as to three. It is also very easy to implement, even where (possibly non-conformal) mappings have given the top boundary an arbitrary shape.

Figure 3 illustrates the computational domain with the top two grid lines marked. If we imagine marching equation (4) (with $\omega = 0$) upwards from these two lines, the initial conditions for Ψ on them should be such that we do not pick up any exponentially growing modes. That is the case only if the values on these two lines

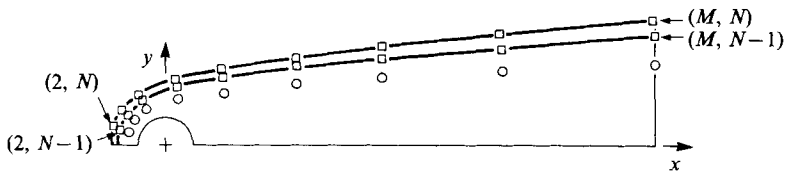

FIGURE 3. Implementation of the boundary condition for Ψ on the top boundary: (,) grid-point indexing; □, grid-point locations on the outermost two grid lines; ○, intersections of vortex rings with the (x, y) plane.

obey a certain set of M linear constraints. With the notation in figure 3, it should be possible to write such constraints as

$$\begin{bmatrix} \Psi_{1,N-1} \\ \Psi_{2,N-1} \\ \vdots \\ \Psi_{M,N-1} \end{bmatrix} = \boldsymbol{A} \begin{bmatrix} \Psi_{1,N} \\ \Psi_{2,N} \\ \vdots \\ \Psi_{M,N} \end{bmatrix}. \tag{9}$$

It remains to determine the matrix $\boldsymbol{A}$. Any solution to (4), with $\omega = 0$ and decaying for increasing η, can be inspected along the top two grid lines to yield a pair of vectors satisfying (9). M such independent pairs, placed side by side, forms matrices $\boldsymbol{B}$ and $\boldsymbol{C}$ satisfying $\boldsymbol{B} = \boldsymbol{AC}$. This relation can then be solved for $\boldsymbol{A}$. One possibility (which gives a well-conditioned matrix $\boldsymbol{C}$) is to consider circular line vortices. The Ψ-fields around such vortex rings are known explicitly, e.g. Batchelor (1967). Placing a sequence of vortex rings as indicated in figure 3 provides all the data needed to solve for $\boldsymbol{A}$. In two dimensions, pairs of point vortices can be similarly used. This matrix $\boldsymbol{A}$ constitutes the bottom-right square block in the matrix in figure 4(*b*) (described below).

It should be noted that the matrix $\boldsymbol{A}$ is 'universal' in the sense that it does not depend on the flow field within the computational domain (or on the Reynolds number). This is not a consequence of any asymptotic assumptions, which get increasingly accurate the further out one moves into an irrotational domain. It relies only on the fact that (1) and (4) become linear when $\omega = 0$. Full accuracy is achieved even when the flow is rotational in the immediate vicinity inside (but not outside) the boundary.

4. Solution of the algebraic system

The discretized equations are nonlinear. A convenient way to order the equations and unknowns is described in F85. It gives a Jacobian matrix with the structure shown in figure 4(*a*). This coefficient matrix is first reduced to roughly half its size by eliminating all entries below the single diagonal (located in the top-right corner block). The new structure is shown in figure 4(*b*). The sizes of the blocks are given both for a general $\mathrm{M} \times \mathrm{N}$ grid and for the 487×163 grid. Standard row pivoted Gaussian elimination was employed for the main banded part. The remaining border elements were then eliminated. Table 1 summarizes the computational resources needed for each Newton iteration.

The (grossly erroneous) $\Psi \equiv 0$ as initial condition sufficed to get convergence at $R = 100$. Subsequent increments of 100 (of 50 very close to the upper limit of $R =$

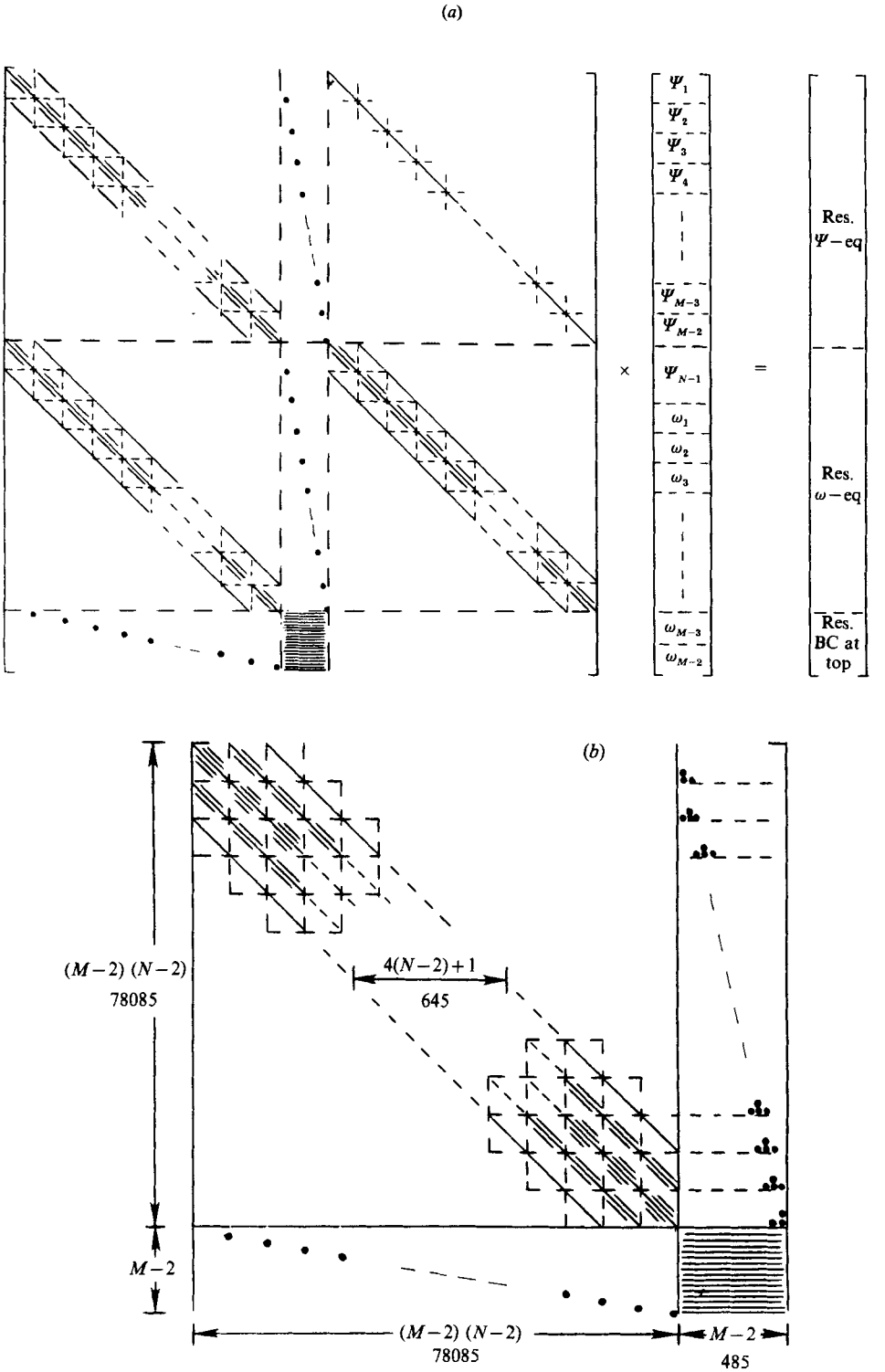

FIGURE 4. (*a*) Structure of the linear system in Newton's method. (*b*) Structure of the reduced Jacobian.

Grid		Computational resources required and performance				
			CPU time, seconds			
Name	Size	Number of arithmetic operations	Generation of each linear system	Linear solver	Sustained Mflop rate	Memory used by linear solver, Mbytes
G1	217×73	4.1×10^9	0.010	46	90	61
G2	325×109	2.1×10^{10}	0.022	191	110	209
G3	487×163	1.1×10^{11}	0.054	828	130	708

TABLE 1. Computational resources required for each Newton iteration. Speeds given for 2-pipe CDC Cyber 205 using 64-bit precision.

5000) with just one iteration at each value of R were sufficient for continuation. Convergence to full machine accuracy at any fixed Reynolds number required an additional 3 to 4 iterations.

5. Equations for the pressure and the drag

In cylindrical (x, y)-coordinates, the pressure satisfies

$$p_x = -\frac{2}{R}\left(\omega_y + \frac{\omega}{y}\right) + \frac{1}{y^2}(\Psi_x \Psi_{yy} - \Psi_y \Psi_{xy}) - \frac{1}{y^3}\Psi_x \Psi_y, \tag{10}$$

$$p_y = \frac{2}{R}\omega_x + \frac{1}{y^2}(\Psi_y \Psi_{xx} - \Psi_x \Psi_{xy}) + \frac{1}{y^3}\Psi_x^2. \tag{11}$$

Changing notation to let x denote complex positions in the (x, y)-plane, an arbitrary conformal mapping $z = z(x)$, $z = \xi + i\eta$, transforms (10), (11) into

$$\begin{aligned} p_\eta = {} & \frac{2}{R}\left\{\omega_\xi - (\mathrm{Im}\, f(x))\cdot\frac{\omega}{|g(x)|\cdot y}\right\} \\ & + \frac{1}{y^2}\{|g(x)|\cdot(\Psi_\xi \Psi_{\eta\eta} - \Psi_\eta \Psi_{\xi\eta}) - (\mathrm{Re}\, h(x))\cdot(\Psi_\xi^2 + \Psi_\eta^2)\} \\ & - \frac{1}{y^3}\{(\mathrm{Re}\, f(x))\,\Psi_\xi \Psi_\eta + (\mathrm{Im}\, f(x))\,\Psi_\eta^2\}, \end{aligned} \tag{12}$$

$$\begin{aligned} p_\eta = {} & \frac{2}{R}\left\{\omega_\xi - (\mathrm{Im}\, f(x))\cdot\frac{\omega}{|g(x)|\cdot y}\right\} \\ & + \frac{1}{y^2}\{|g(x)|\cdot(\Psi_\eta \Psi_{\xi\xi} - \Psi_\xi \Psi_{\xi\eta}) - (\mathrm{Im}\, h(x))\cdot(\Psi_\xi^2 + \Psi_\eta^2)\} \\ & + \frac{1}{y^3}\{(\mathrm{Re}\, f(x))\,\Psi_\xi^2 + (\mathrm{Im}\, f(x))\,\Psi_\xi \Psi_\eta\}, \end{aligned} \tag{13}$$

where

$$f(x) = \frac{\mathrm{d}z}{\mathrm{d}x}, \quad g(x) = \left(\frac{\mathrm{d}z}{\mathrm{d}x}\right)^2, \quad h(x) = \frac{\overline{\mathrm{d}^2 z}}{\mathrm{d}x^2}\cdot\frac{g(x)}{|g(x)|}. \tag{14}$$

With the mapping (3), $f(x) = \frac{1}{2}(x^{-\frac{1}{2}} - x^{-\frac{3}{2}})$ etc.

It is conventional to define a 'non-dimensional' pressure P as

$$P = \frac{p - p_\infty}{\frac{1}{2}\rho U_\infty^2}, \tag{15}$$

where p is defined as in (10) and (11), p_∞ is the pressure at infinity (set to 0), ρ the density and U_∞ the fluid velocity at infinity (both set to 1). After assigning the pressure to be zero at the top-right corner of the computational domain, (13) was used to find P $(= 2p)$ along the right (outflow) boundary. Integrating (12) (for decreasing ξ) then provided the results across the complete computational domain.

The drag coefficient C_D is the sum of two components, one arising from the viscous forces and the other from the pressure distribution over the sphere. These components take a particularly simple form in polar (r, θ)-coordinates:

$$C_V = -\frac{8}{R}\int_0^\pi \omega_{r=1} \sin^2\theta \, d\theta \tag{16}$$

and

$$C_P = \frac{4}{R}\int_0^\pi \left\{\left(\omega + \frac{\partial\omega}{\partial r}\right)_{r=1} \sin^2\theta\right\} d\theta. \tag{17}$$

In (ξ, η)-coordinates, these equations become

$$C_V = -\frac{8}{R}\int_0^2 \omega_{\eta=0}\, \xi^2 \{1 - (\tfrac{1}{2}\xi)^2\}^{\frac{1}{2}} d\xi \tag{18}$$

and

$$C_P = \frac{4}{R}\int_0^2 \left\{\frac{\partial\omega}{\partial\eta}\right\}_{\eta=0} \xi^2 \{1 - (\tfrac{1}{2}\xi)^2\}\, d\xi - \tfrac{1}{2}C_V. \tag{19}$$

6. Tests of accuracy

Main sources of errors include: (i) machine rounding errors; (ii) truncation errors arising from finite differencing of derivatives; and (iii) boundary conditions simulating infinite domains implemented at a finite distance.

The first error source proved negligible with use of 64-bit floating point precision. After the Newton iterations had converged, future iterations displayed random fluctuations in Ψ and ω, typically only about 10^{-10}.

Regarding the second source, table 2 shows how the dimensions of the recirculation region (length measured from the centre of the sphere, width across the full wake) and the drag coefficient vary between the different grids for different Reynolds numbers. (Computations on grid G1 could be continued only to $R = 2300$ and on G2 to $R = 3725$ owing to the emergence of spurious singularities.) The results are generally consistent with what one should expect from a second order scheme under successive mesh refinements with factors of $\frac{2}{3}$. The error level should approximately halve at each refinement. The error levels appear to be well below 1%.

The errors arising from the outer boundary conditions were tested by increasing the extent of grid G1 from 217×73 to 225×81 and 233×89 points. The three domains are denoted D1, D2 and D3 respectively; all discretization levels, grid transformations etc. were left unchanged. Figure 5 compares these extended domains (D2 and D3) to the basic one (D1) (The grid shown in D1 is the same 55×19 grid as

	Wake length			Wake width			Drag coefficient		
R	G1	G2	G3	G1	G2	G3	G1	G2	G3
100	2.747	—	—	1.818	—	—	1.085	—	—
200	3.871	—	—	2.264	—	—	0.768	—	—
500	5.062	5.065	—	2.590	2.601	—	0.481	0.482	—
1000	5.489	5.497	5.502	3.285	3.303	3.312	0.319	0.319	0.319
2000	6.038	5.987	5.983	4.220	4.192	4.196	0.196	0.200	0.200
5000	—	—	6.797	—	—	5.462	—	—	0.113

TABLE 2. Wake dimensions (length measured from centre of sphere, width across the full wake) as functions of computational grid density

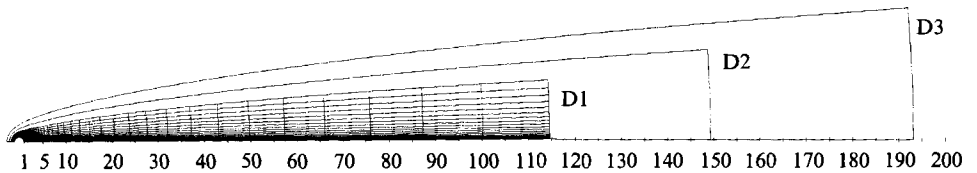

FIGURE 5. Comparison between the computational domains D1, D2 and D3.

	Wake length			Wake width			Drag coefficient		
R	D1	D2	D3	D1	D2	D3	D1	D2	D3
100	2.747	2.744	2.744	1.818	1.816	1.816	1.085	1.085	1.084
200	3.871	3.868	3.867	2.264	2.262	2.262	0.768	0.768	0.768
500	5.062	5.060	5.058	2.590	2.587	2.586	0.481	0.482	0.482
1000	5.489	5.484	5.481	3.285	3.279	3.276	0.319	0.320	0.320
2000	6.038	6.027	6.016	4.220	4.206	4.195	0.196	0.197	0.198
5000	—	—	—	—	—	—	—	—	—

TABLE 3. Wake dimensions (length measured from centre of sphere, width across the full wake) as functions of the position of the outer boundaries. All results are based on the grids with the same density as G1 (i.e. $\Delta\zeta = \frac{1}{36}$, $\Delta\kappa = \frac{1}{54}$).

shown in figure 2.) The results in table 3 indicate that the basic domain is of sufficient extent for errors again to be less than about 1%.

7. Results

Figure 6 shows the streamlines and figure 7 contours of equal vorticity at Reynolds numbers 100, 200, 500, 1000, 2000 and 5000. Details of the vorticity fields near the sphere are shown in figure 8 for Reynolds numbers 100, 500 and 5000. For Ψ, the contour values are

$$\begin{cases} 0, 0.2 \\ 1.0, 4.0, 9.0, 16.0 \ldots \\ -0.2, -0.4, -0.6, -0.8, -1.0, \ldots, \end{cases} \tag{20}$$

and for ω

$$\pm\{0.1, 0.2, 0.3, 0.5, 0.7, 1, 2, 3, 5, 7, 10, 20, 30, 50\}. \tag{21}$$

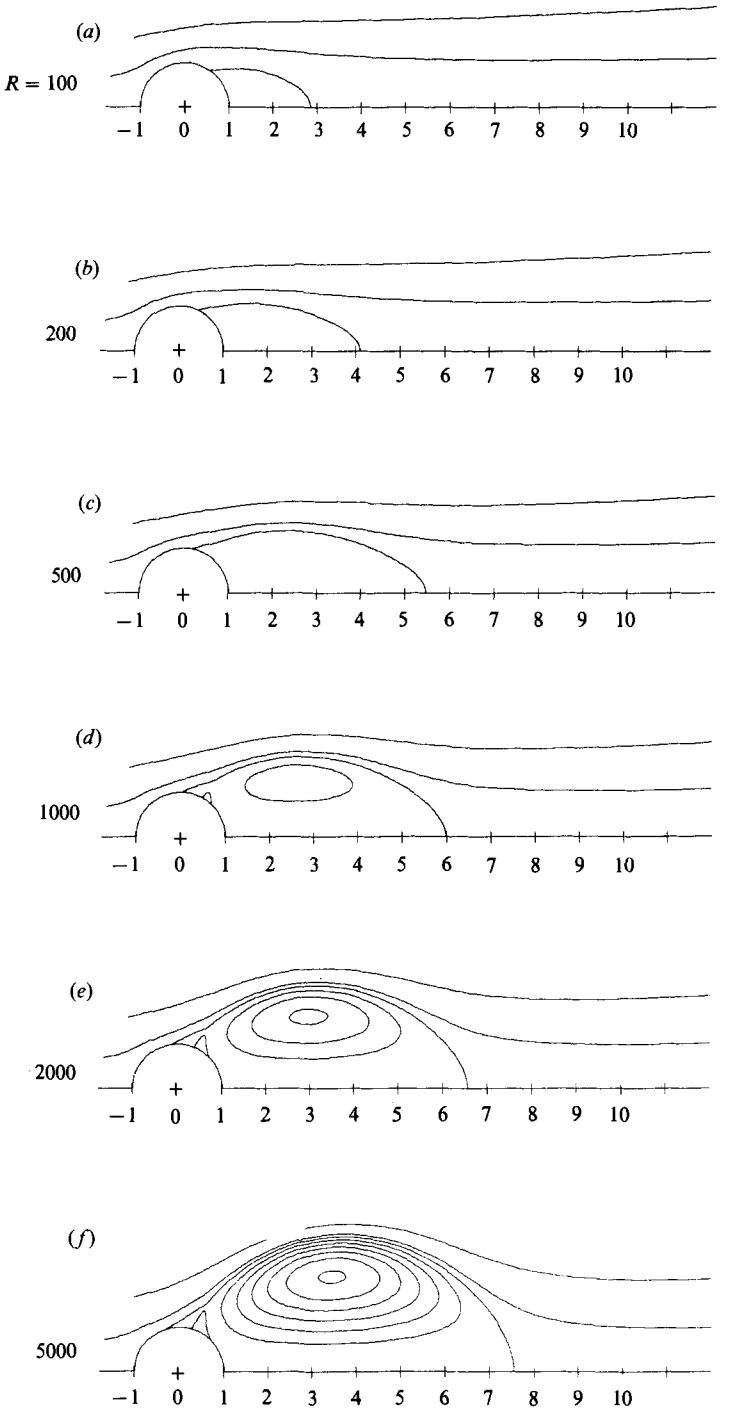

FIGURE 6. Streamlines.

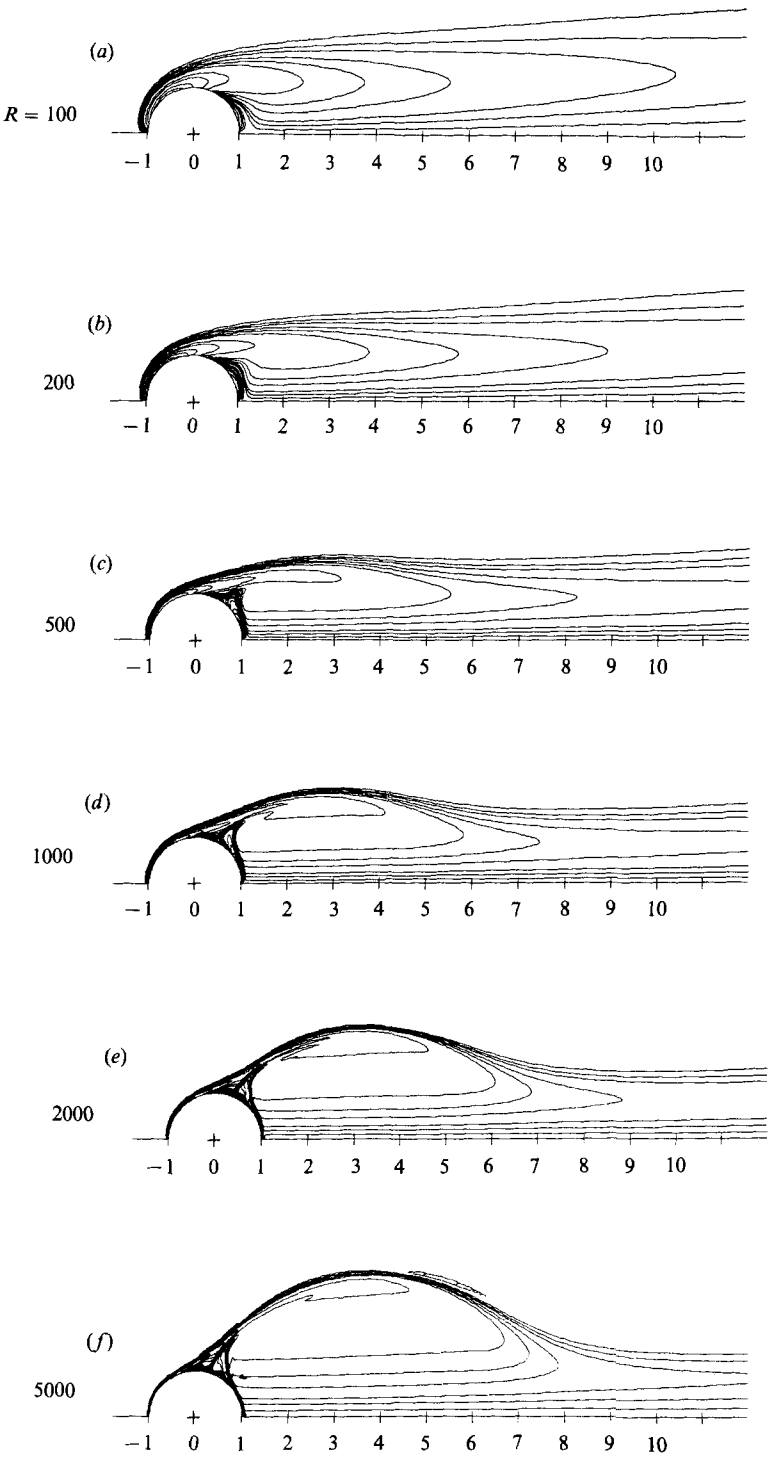

FIGURE 7. Contours of constant vorticity.

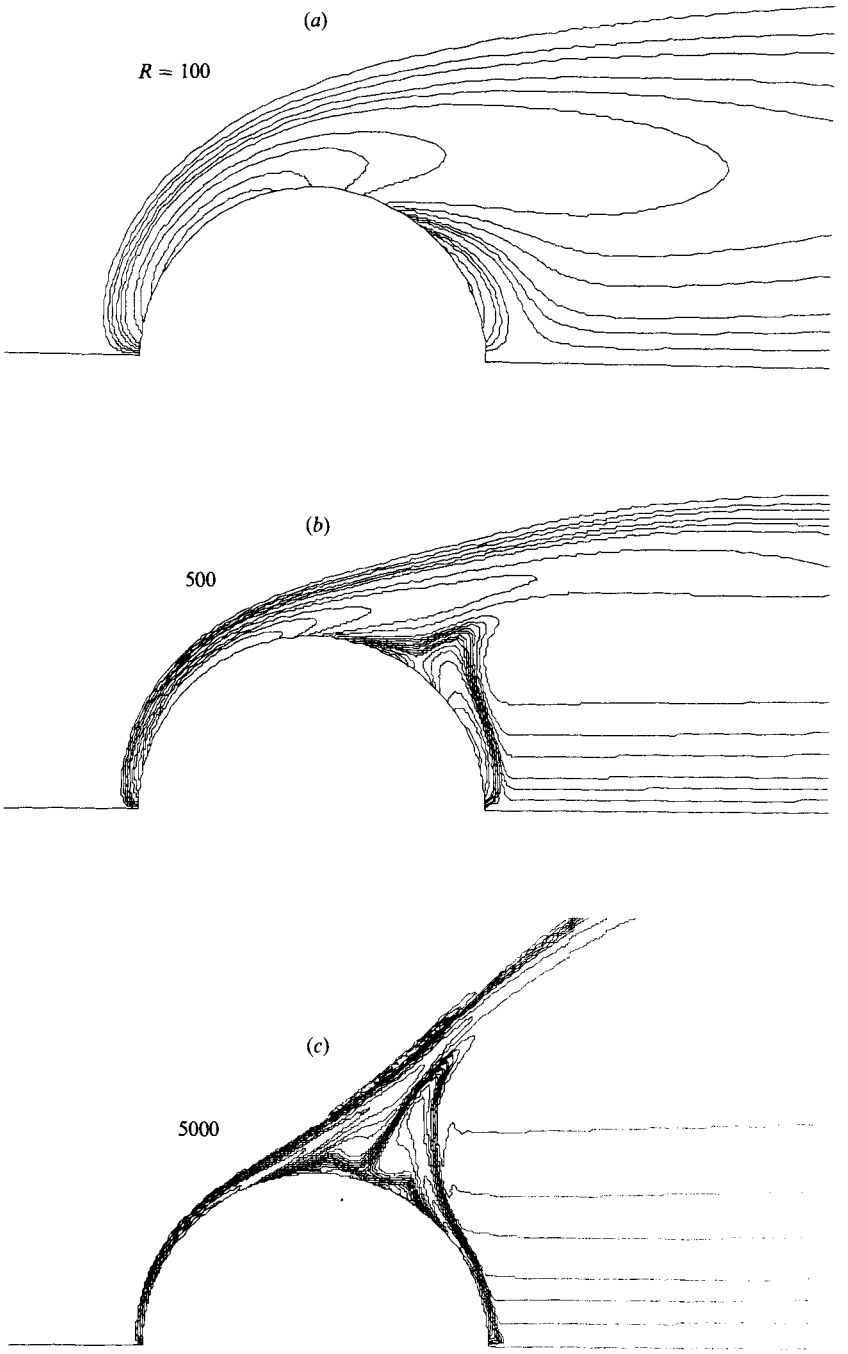

FIGURE 8. Contours of constant vorticity near the sphere.

To provide a better impression of the structure of the wake, figure 9 displays the vorticity fields as surface projections. The figures are based on grid G1 for $R = 100$, 200, on G2 for $R = 500$ and on G3 for $R = 1000$, 2000 and 5000.

At the higher Reynolds numbers, the vorticity distribution in the wake bubble resembles that of a Hill's spherical vortex (e.g. Batchelor 1967). Such vortices have

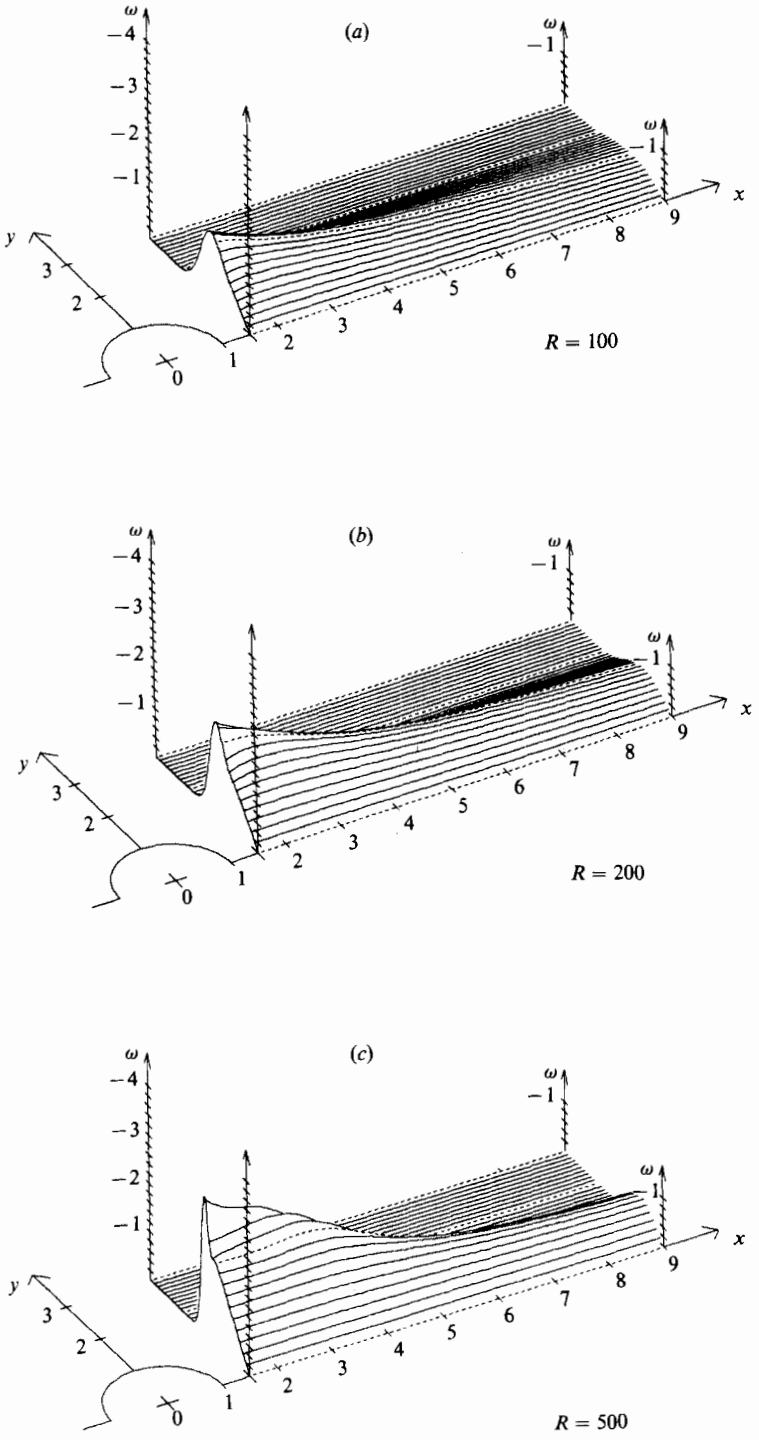

FIGURE 9(a-c). For caption see facing page.

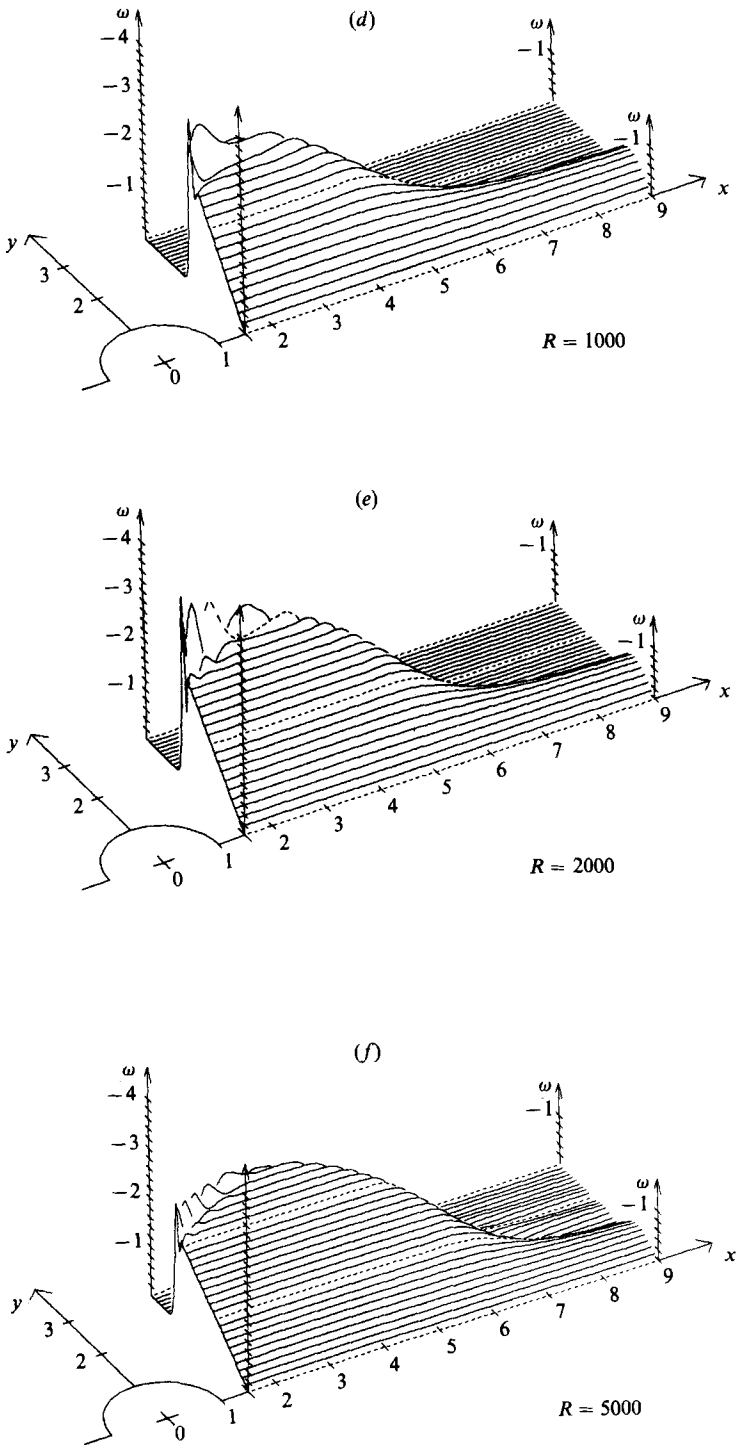

FIGURE 9. Distribution of vorticity in the wake at different Reynolds numbers.

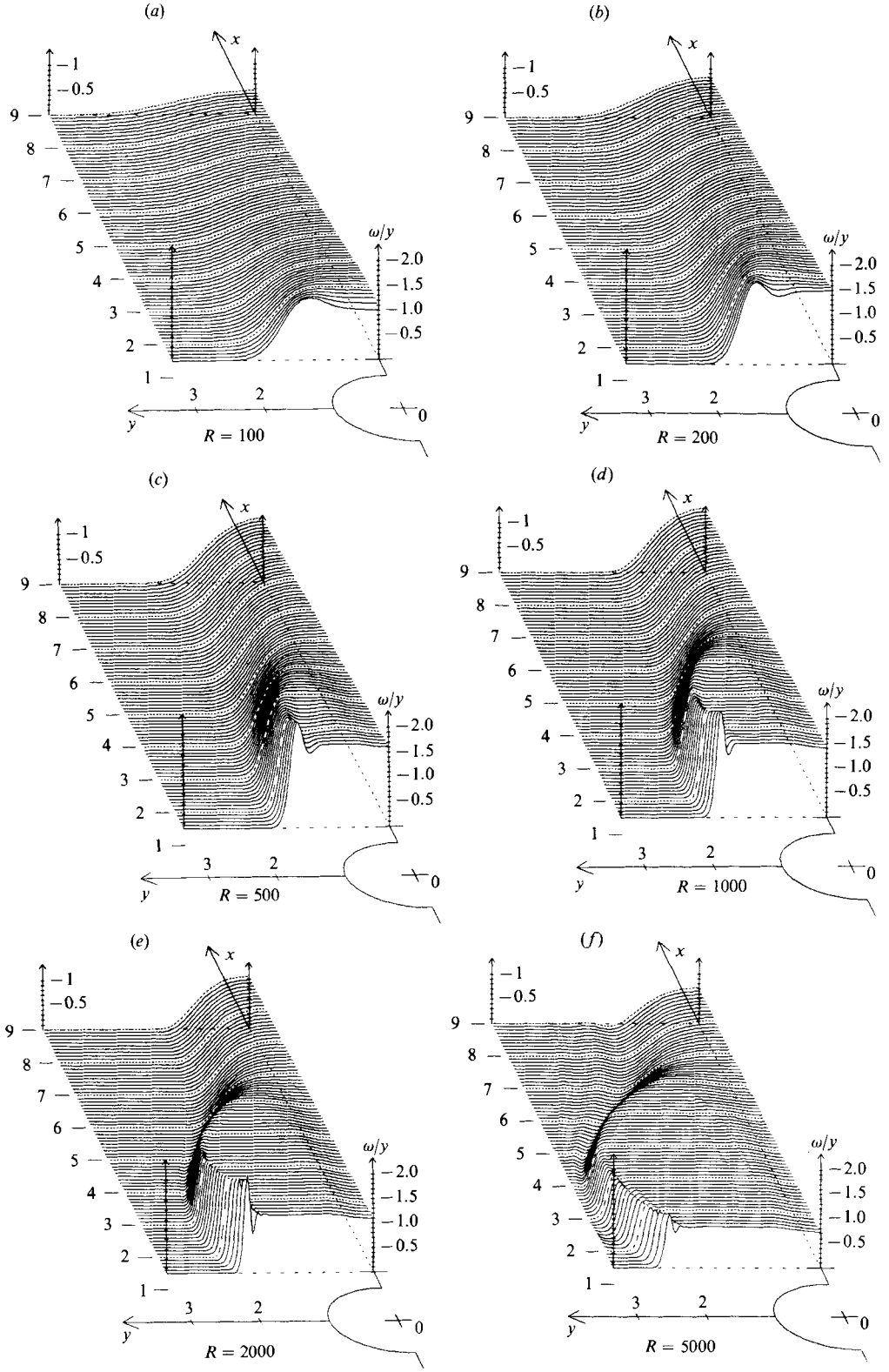

FIGURE 10. Values of ω/y in the wake behind the sphere at different Reynolds numbers.

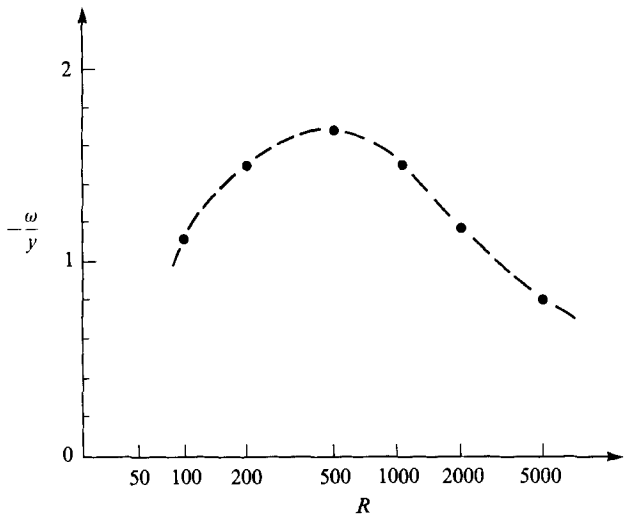

FIGURE 11. Levels of ω/y within the recirculation region for different Reynolds numbers.

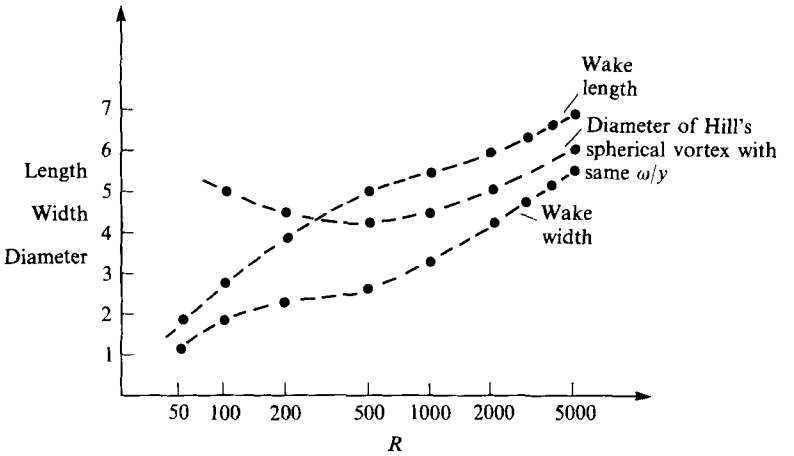

FIGURE 12. Length and width of the recirculation region for different Reynolds numbers compared to the diameters of Hill's spherical vortices with the same observed values for ω/y.

ω/y = const. inside a spherical flow domain, $\omega = 0$ outside it. This resemblance can be seen still more clearly in figure 10 which displays ω/y instead of ω alone.

If a Hill's spherical vortex is travelling with unit speed, its diameter d satisfies the relation

$$d = \{30/|\omega/y|\}^{\frac{1}{2}}. \tag{22}$$

The constant levels of ω/y observed within the wake bubbles are shown in figure 11. Corresponding values for d are shown in figure 12 together with the wake length and width (measured from the centre of the body and across the full wake respectively). If the limit is indeed of the spherical vortex form and grows to infinite size, all the three curves in figure 12 should ultimately approach each other.

Spurious mesh oscillations were noticeable for the vorticity near the leading edge of the wake bubble in the $R = 5000$ case. For increased clarity in figure 7(f),

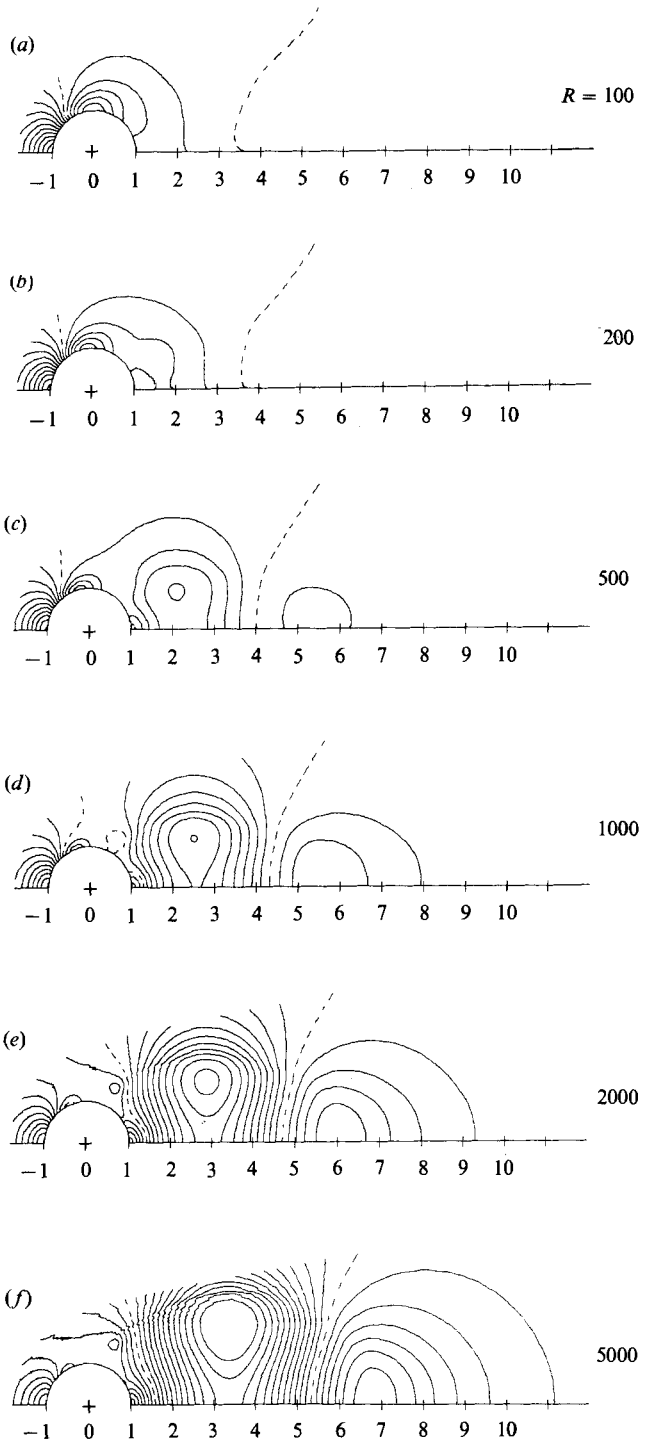

FIGURE 13. Pressure fields.

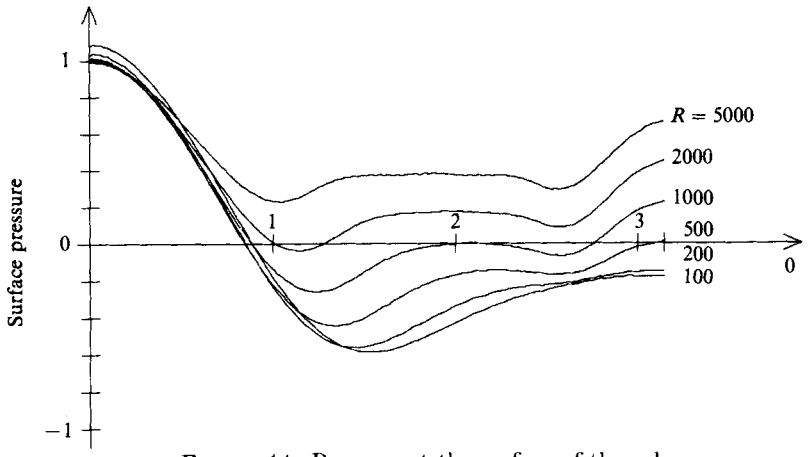

FIGURE 14. Pressure at the surface of the sphere.

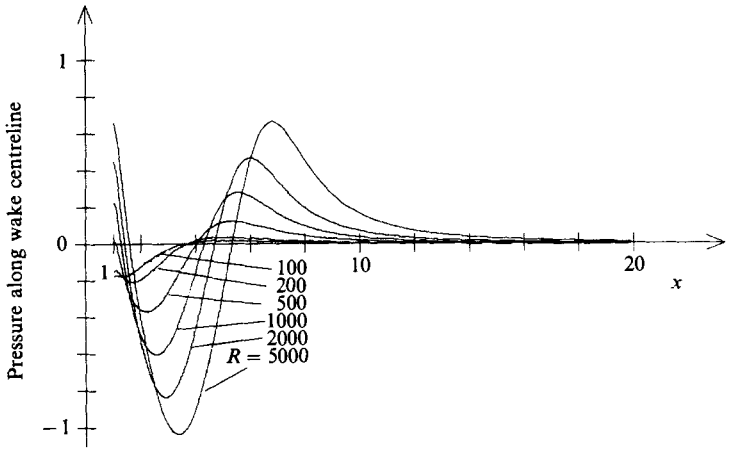

FIGURE 15. Pressure along the centre of the wake.

R	C_V	C_P	C_D
100	0.5087	0.5765	1.0852
200	0.4093	0.3590	0.7683
500	0.3034	0.1784	0.4818
1000	0.2234	0.0952	0.3187
2000	0.1531	0.0473	0.2005
5000	0.0949	0.0183	0.1131

TABLE 4. Drag coefficients C_V, C_P and C_D calculated on the basic domain with the highest-resolution grid used at each Reynolds number

$8(c)$, $9(f)$ and $10(f)$, the vorticity data (on G3) were damped by three times applying the smoothing operator with stencil

$$\begin{bmatrix} 1 & 2 & 1 \\ 2 & 4 & 2 \\ 1 & 2 & 1 \end{bmatrix} \Big/ 16. \tag{23}$$

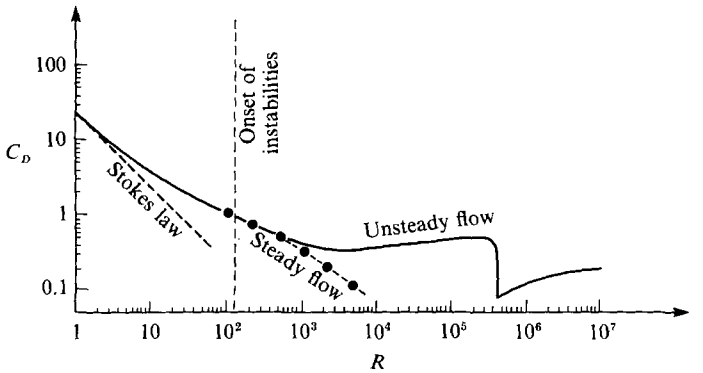

FIGURE 16. Experimental values for C_D compared to Stokes law and to the present results for steady flow.

The pressure outside the sphere, over its surface and along the centreline of the wake are shown in figures 13, 14 and 15 respectively. The contour lines in figure 13 differ by $\Delta P = 0.1$; the dotted lines correspond to $P = 0$.

The values obtained for C_V, C_P and C_D $(=C_V+C_P)$ for various Reynolds numbers are given in table 4 (based on the finest grid used at that Reynolds number). In figure 16, the values for C_D are compared to a summary of experimental (unsteady) results compiled by Clift, Grace & Weber (1978; as reported in their figure 5.2).

8. Conclusions

Calculations leading up to those presented in F85 for the two-dimensional case of flow past a cylinder have led to a reassessment of models for wake structures. New models, based on the wide wakes which were observed, have been considered by Peregrine (1985) and Smith (1985, 1986, 1987). For the three-dimensional case of flow past a sphere, fewer attempts at modelling have been made in the past. Our present calculation suggests that the wake will take the form of a perturbed Hill's spherical vortex. A finite-sized wake of this kind was proposed by Batchelor (1956).

Unless advances are made in the area of active flow control, no immediate practical applications are anticipated for the (very low drag) flows we have observed. Somehow maintaining axial symmetry is unlikely to suffice since Hill's spherical vortices for Euler flow are unstable even in that case (Pozrikidis 1986).

REFERENCES

BATCHELOR, G. K. 1956 A proposal concerning laminar wakes behind bluff bodies at large Reynolds number. *J. Fluid Mech.* **1**, 388.

BATCHELOR, G. K. 1967 *An Introduction to Fluid Dynamics.* Cambridge University Press.

CLIFT, R., GRACE, J. R. & WEBER, M. E. 1978 *Bubbles, Drops and Particles.* Academic.

FORNBERG, B. 1985 Steady viscous flow past a circular cylinder up to Reynolds number 600. *J. Comp. Phys.* **61**, 297.

FORNBERG, B. 1987 Steady viscous flow past a cylinder and a sphere at high Reynolds numbers. In *Boundary-Layer Separation* (ed. F. T. Smith & S. N. Brown), p. 3. Springer.

LE CLAIR, B. P., HAMIELEC, A. E. & PRUPPACHER, H. R. 1970 A numerical study of the drag on a sphere at low and intermediate Reynolds numbers. *J. Atmos. Sci.* **27**, 308.

PEREGRINE, D. H. 1985 A note on the steady high-Reynolds-number flow about a circular cylinder. *J. Fluid Mech.* **157**, 493.

POZRIKIDIS, C. 1986 The nonlinear instability of Hill's vortex. *J. Fluid Mech.* **168**, 337.

SMITH, F. T. 1985 A structure for laminar flow past a bluff body at high Reynolds number. *J. Fluid Mech.* **155**, 175.

SMITH, F. T. 1986 Concerning inviscid solutions for large-scale separated flows *J. Engng Maths* **20**, 271.

SMITH, F. T. 1987 Separating flow: Small-scale, large-scale and nonlinear unsteady effects. In *Boundary-Layer Separation* (ed. F. T. Smith & S. N. Brown), p. 331. Springer.

TA, P. L. 1975 Étude numérique de l'écoulement d'un fluide visqueux incompressible autour d'un cylindre fixe ou en rotation. Effet Magnus. *J. Méc.* **14**, 109.

WOO, S. W. 1971 Simultaneous free and forced convection around submerged cylinders and spheres. Ph.D. thesis, McMaster University, Hamilton, Ontario.